

Thermal radiation spin torque on magneto-optical media

Xingyu Gao,¹ Chinmay Khandekar,² Zubin Jacob,^{2,*} and Tongcang Li^{1,2,3,†}

¹*Department of Physics and Astronomy, Purdue University, West Lafayette, Indiana 47907, USA*

²*Birck Nanotechnology Center, School of Electrical and Computer Engineering,
College of Engineering, Purdue University, West Lafayette, IN 47907, USA*

³*Purdue Quantum Science and Engineering Institute,
Purdue University, West Lafayette, Indiana 47907, USA*

(Dated: March 12, 2022)

Spin and orbital angular momentum of light play a central role in nanophotonics as well as topological electrodynamics. Here, we show that the thermal radiation from finite-sized bodies comprising of nonreciprocal magneto-optical materials carries a net angular momentum flux. Such angular momentum loss gives a nontrivial temperature-dependent torque on bodies which can be measured experimentally. We combine Rytov's fluctuational electrodynamics with the theory of optical angular momentum to calculate the thermal radiation torque on finite-size nonreciprocal objects. We prove that a single magneto-optical cubic particle in non-equilibrium with its surroundings experiences a torque in the presence of an applied magnetic field (T-symmetry breaking). Furthermore, even in global thermal equilibrium, two particles with misaligned gyrotropic axes experience equal magnitude torques with opposite signs which tend to align their gyrotropic axes parallel to each other. Our results are universally applicable to semiconductors like InSb (magneto-plasmas) as well as Weyl semi-metals which exhibit the anomalous Hall effect (gyrotropy) at infrared frequencies. Our work paves the way towards near-field angular momentum transfer mediated by thermal fluctuations for nanoscale devices.

I. INTRODUCTION

Nanoscale radiative transfer plays an important role in a wide range of scientific and engineering disciplines. It has a variety of promising applications including energy conversion [1, 2], thermal rectification [3, 4], near-field spectroscopy [5, 6] and near-field super-Planckian emission [7–10] etc. Over the past few years, most of the investigations in this field focused on the near-field heat transfer i.e. energy transferred between various bodies in thermal non-equilibrium. It should be emphasized that in global equilibrium there is no net flow of energy in these systems [11–13]. Our goal in this paper is to explore concepts beyond energy i.e. angular momentum which can be exchanged/transferred between bodies even in global thermal equilibrium. Thus our work is closely connected to the concept of Casimir torque [14] in non-reciprocal materials at finite temperatures.

Thermal spin photonics is an emerging research area that combines the thermal radiation and the spin angular momentum (SAM) of light [15–18]. Non-reciprocal materials such as semiconductors in external magnetic fields [19–21] and Weyl semimetals [22] are of great interest in the context of thermal spin photonics as they break the time reversal symmetry and lead to many interesting effects [23–28]. Recent work showed that the thermal radiation of a non-reciprocal medium carries angular momentum (AM) [29]. There also exist uniquely new Kirchhoff's laws of thermal radiation from non-reciprocal media [30] that are intimately tied to spin angular mo-

mentum of thermal radiation. However, the geometry of these investigations were limited to a semi-infinite half-space slab due to the computational difficulty of the analytical approach to other complex geometries. Recently, lots of progress has been made on numerical approach in the context of near-field heat transfer with nontrivial geometries. Those computational tools include scattering matrix [31, 32], boundary-element methods [33, 34], volume-integral-equation methods [35], and the thermal discrete dipole approximation method (TDDA) [36–38], etc. However, so far none of them has been used for analyzing radiative angular momentum transfer of non-reciprocal bodies. Here, we primarily aim to explore thermal AM radiation in the near-field and far-field of finite-size nonreciprocal objects.

We explore the AM-resolved thermal radiation features in a system comprising of magneto-optical bodies in external magnetic fields (as shown in Figure 1). Magneto-optic (MO) media, such as doped Indium Antimonide (InSb), become gyroelectric objects in the presence of magnetic fields and hence exhibit stable non-reciprocity that can be controlled by changing the magnitudes and the directions of the magnetic fields [25, 27]. We find that the thermal radiation from a single gyroelectric body carries a net AM flux along its gyrotropic axis when the system is out of equilibrium with vacuum and thus feels a torque along the opposite direction. More interestingly, we also find that for a two-body system with misaligned gyrotropic axes, AM transfer between two bodies can occur regardless of the global thermal equilibrium. The AM transfer results in a torque with the same magnitude but opposite signs on two bodies trying to align the gyrotropic axes parallel to each other. Moreover, the total torque on the combined system is zero, which indi-

* zjacob@purdue.edu

† tcli@purdue.edu

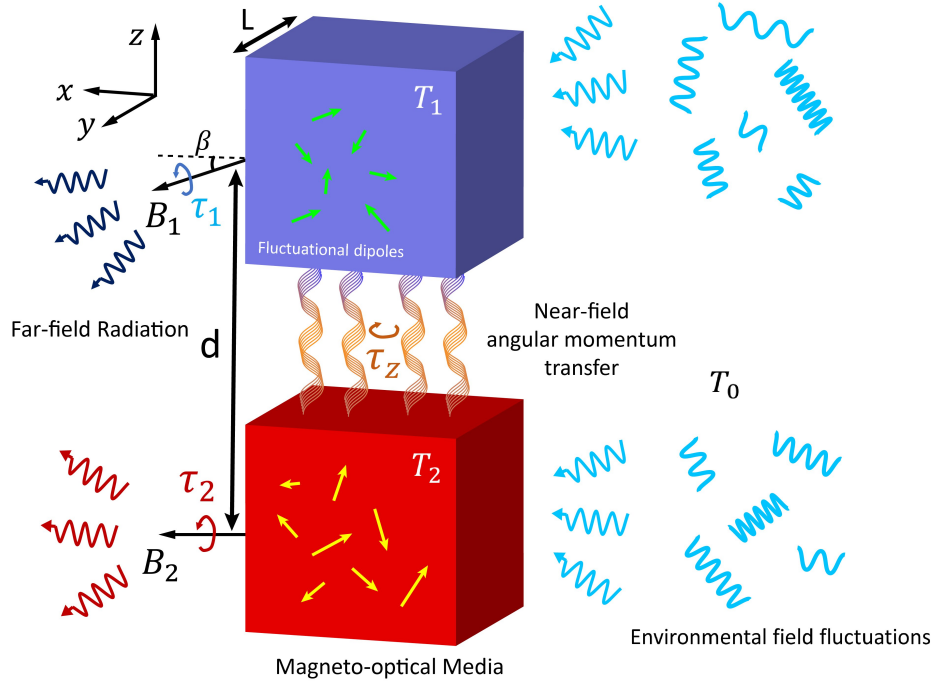


Figure 1. (Color online) Schematic of the radiative AM transfer in a two-body MO system in the presence of external magnetic fields. Two cubes are separated by a distance d (center to center distance) and they have the same size L . T_1 , T_2 and T_0 denote the temperatures of the top cube, bottom cube and environment, respectively.

cates that there is no net AM flux transferred to the far field, satisfying the detailed balance of the AM flux at equilibrium.

In this work, we utilize fluctuational electrodynamics (FE) that combines the Maxwell electromagnetic theory of angular momentum and the fluctuational-dissipation theorem (FDT) [39]. In particular, our numerical approach is generalized from the TDDA method by a recent work studying the thermal emission in magneto-optical (MO) systems [38]. In that work, the authors proved the validity of the TDDA method for optically anisotropic systems that can be described by an arbitrary electric permittivity tensor (with $\mu = 1$). We extend the TDDA approach to describe the thermal AM flux at the near-field and far-field of finite nonreciprocal bodies. Moreover, we apply our TDDA approach on exploring the thermal emission of AM in MO systems and reveal the origins of the thermal AM torques when the system is out of equilibrium by computing the AM flux across different planes.

We also demonstrate the nontrivial role of non-reciprocity in causing an equilibrium torque in a system which is at global thermal equilibrium. Such equilibrium torque is non-intuitive but important since it opens a degree of freedom for directional radiative AM transfer. Experimental demonstration of such an effect requires misaligned magnetic fields which can be generated using spatial gradients of 2D magnetic fields on nanoscale objects. Our work provides a way to explore many in-

teresting effects in the context of thermal AM in non-reciprocal systems. We emphasize that our system under consideration is significantly subwavelength functioning in the dipolar approximation. Therefore, the contribution of angular momentum is dominated by spin as opposed to orbital angular momentum. This observation is consistent with recent experiments in ion traps where orbital angular momentum has been shown to couple only to quadrupolar optical transitions, not dipolar optical transitions [40, 41]. To emphasize the analogy with spin transfer torque in nanoelectronics [42, 43], we term our phenomenon as thermal photonic spin transfer torque. We also note that our work is applicable not only to magnetized-plasmas like InSb but also to Weyl semi-metal particles which show the anomalous Hall effect (non-reciprocity) without an applied magnetic field [44–46].

The rest of the paper will be organized as follows. In Sec. II, we show our theoretical formalism of the TDDA method to describe the radiative AM transfer at the near-field and far-field of MO objects. In Sec. III, we discuss our numerical results obtained by our TDDA approach. We separate our discussion into the single-cube case and two-cube case. For each case, we consider both the thermal equilibrium and non-equilibrium conditions. In Sec. IV, we summarize our observations in Sec. III and conclude the paper with some additional remarks.

II. ANGULAR MOMENTUM IN FLUCTUATIONAL ELECTRODYNAMICS

A. Radiative Angular Momentum Flux

We consider a single- or two-cube system made of non-reciprocal materials shown in Figure 1. We focus on the AM-resolved thermal radiation on the vacuum side of the systems. For this purpose, momentum and AM will be studied in the context of the thermal radiation. These quantities are important because they are conserved and thus follow the conservation laws. First, the radiative momentum at the observation point can be quantified by Poynting flux \mathbf{P} and the momentum flux density $\mathbf{\Sigma}$ [47]:

$$\langle \mathbf{P} \rangle = \langle \mathbf{E} \times \mathbf{H} \rangle, \quad (1)$$

$$\begin{aligned} \langle \mathbf{\Sigma} \rangle = & -\epsilon_0 \langle \mathbf{E} \otimes \mathbf{E} \rangle - \mu_0 \langle \mathbf{H} \otimes \mathbf{H} \rangle \\ & + \frac{1}{2} \epsilon_0 \text{Tr} \{ \langle \mathbf{E} \otimes \mathbf{E} \rangle \} \mathbb{I} + \frac{1}{2} \mu_0 \text{Tr} \{ \langle \mathbf{H} \otimes \mathbf{H} \rangle \} \mathbb{I} \end{aligned} \quad (2)$$

where \otimes denotes the outer product of two vectors, and $\langle \dots \rangle$ denotes the thermodynamic ensemble average. All the quantities in Eq. 1 and Eq. 2 are dependent on the position \mathbf{r} and time t . The radiation momentum transfer leads to a force \mathbf{F} on the objects that can be obtained by the conservation law of momentum:

$$\int_S \langle \Sigma_{ij}(\mathbf{r}, t) \rangle dS_j = -\frac{\partial}{\partial t} \left(\int_V \langle \mathbf{P}(\mathbf{r}, t) \rangle dV \right)_i = -\langle F_i \rangle. \quad (3)$$

Similarly, the radiation AM can be quantified by AM density \mathbf{J} and AM flux density \mathbf{M} [47]:

$$\langle \mathbf{J}(\mathbf{r}, t) \rangle = \mathbf{r} \times \langle \mathbf{E}(\mathbf{r}, t) \times \mathbf{H}(\mathbf{r}, t) \rangle \quad (4)$$

$$\langle \mathbf{M}(\mathbf{r}, t) \rangle = \mathbf{r} \times \langle \mathbf{\Sigma}(\mathbf{r}, t) \rangle \quad (5)$$

which is given by the cross product of the position with the Maxwell stress tensor. They also satisfy the continuity equation

$$\frac{\partial}{\partial t} J_i + \frac{\partial}{\partial x_l} M_{li} = 0. \quad (6)$$

A nonreciprocal medium can lead to a nonzero radiation AM flux and thus results in a torque τ on objects. This torque can be obtained by the conservation law of AM, which is the integral form of the continuity equation in Eq. 6:

$$\int_S \langle M_{ij}(\mathbf{r}, t) \rangle dS_j = -\frac{\partial}{\partial t} \left(\int_V \langle \mathbf{J}(\mathbf{r}, t) \rangle dV \right)_i = -\langle \tau_i \rangle. \quad (7)$$

All the quantities throughout the manuscript are described in SI units. Next, we express the physical quantities in terms of their Fourier transforms, such as

$$\mathbf{E}(t) = \int_{-\infty}^{\infty} \frac{d\omega}{2\pi} \mathbf{E}(\omega) e^{-i\omega t}, \quad (8)$$

$$\mathbf{H}(t) = \int_{-\infty}^{\infty} \frac{d\omega}{2\pi} \mathbf{H}(\omega) e^{-i\omega t}. \quad (9)$$

for electromagnetic field and similarly for other quantities. Then above quantities $\mathbf{Q} = \{\mathbf{\Sigma}, \mathbf{M}, \mathbf{F}, \tau\}$ are to be integrated over frequency to obtain the total flux/force/torque as $\mathbf{Q} = \int_{-\infty}^{\infty} \frac{d\omega}{2\pi} \mathbf{Q}(\omega) e^{-i\omega t}$. The electromagnetic field correlations required for calculating densities and flux rates above are obtained from the fluctuation-dissipation theorem (FDT). We can separate the contributions into two parts: the first one accounts for the fluctuations of particle dipole moments that will further induce electromagnetic field; the second part involves environmental field fluctuations. The FDT in our case gives [48]

$$\begin{aligned} \langle p_{f,i}(\omega) p_{f,j}^*(\omega') \rangle = & 2\pi \hbar \epsilon_0 \delta(\omega - \omega') \\ & \times \text{Im} \{ \alpha_{ij}(\omega) \} (1 + 2n_p(\omega)) \end{aligned} \quad (10)$$

for the electric dipole fluctuations and

$$\begin{aligned} \langle E_{f,i}(\mathbf{r}, \omega) E_{f,j}^*(\mathbf{r}', \omega') \rangle = & 2\pi \frac{\hbar k_0^2}{\epsilon_0} \delta(\omega - \omega') \\ & \times \text{Im} \{ G_{EE,ij}(\mathbf{r}, \mathbf{r}') \} (1 + 2n_0(\omega)) \end{aligned} \quad (11)$$

for the environmental electric-field fluctuations, where $k_0 = \omega/c$ is the magnitude of the vacuum wave vector. Here $\hat{\alpha}$ is the polarizability of the objects and $\mathbf{G}_{EE}(\mathbf{r}, \mathbf{r}')$ is the free space electric-electric dyadic Green's tensor [48]. The temperature of the particle T_p and the vacuum T_0 enter these expressions through the Bose-Einstein distribution $n_l(\omega) = 1/(e^{\hbar\omega/k_B T_l} - 1)$.

B. Numerical Approach: Thermal Discrete Dipole Approximation

To numerically compute the physical quantities introduced in Eq. 5 and Eq. 7, we extend the TDDA approach for MO objects based on Ref. [38]. Here we summarize the important equations we have developed. More details can be found in Appendix A.

Considering a two-body system interacting with a thermal bath, we use a collection N_p (for object p) electric point dipoles to describe the system. Each dipole is characterized by a volume $V_{i,p}$ and a polarizability tensor $\hat{\alpha}_{i,p}$, where $p=1,2$ denotes the body that the dipole belongs to and $i=1,2,\dots,N_p$ indicates the i -th subvolume in that object. We group the electric dipoles and electric fields

inside bodies in a compact form:

$$\begin{aligned} \bar{\mathbf{P}} &= \begin{pmatrix} \bar{\mathbf{P}}_1 \\ \bar{\mathbf{P}}_2 \end{pmatrix}; \quad \bar{\mathbf{P}}_1 = \begin{pmatrix} \mathbf{P}_{1,1} \\ \vdots \\ \mathbf{P}_{N_1,1} \end{pmatrix}, \bar{\mathbf{P}}_2 = \begin{pmatrix} \mathbf{P}_{1,2} \\ \vdots \\ \mathbf{P}_{N_2,2} \end{pmatrix} \\ \bar{\mathbf{E}} &= \begin{pmatrix} \bar{\mathbf{E}}_1 \\ \bar{\mathbf{E}}_2 \end{pmatrix}; \quad \bar{\mathbf{E}}_1 = \begin{pmatrix} \mathbf{E}_{1,1} \\ \vdots \\ \mathbf{E}_{N_1,1} \end{pmatrix}, \bar{\mathbf{E}}_2 = \begin{pmatrix} \mathbf{E}_{1,2} \\ \vdots \\ \mathbf{E}_{N_2,2} \end{pmatrix}. \end{aligned} \quad (12)$$

The notation $\bar{\mathbf{C}}$ ($\mathbf{C} = \{\mathbf{p}, \mathbf{E}, \dots\}$) indicates that the dipoles or the field is inside bodies and in the following discussion, we denote \mathbf{C} without the overhead bar label as the quantities in vacuum.

To obtain the total radiative AM flux at the near field or far field (obsevation point), we need to compute the statistical average of the AM flux density introduced in Eq. (5). Making use of the Fourier transforms, the average of the AM flux density can be expressed as

$$\begin{aligned} \langle \mathbf{M}(\mathbf{r}) \rangle &= -2 \int_0^\infty \frac{d\omega}{2\pi} \int_{-\infty}^\infty \frac{d\omega'}{2\pi} \mathbf{r} \times \\ &\quad \text{Re}[\epsilon_0 \langle \mathbf{E}(\mathbf{r}, \omega) \otimes \mathbf{E}^*(\mathbf{r}, \omega') \rangle e^{-i(\omega - \omega')t} \\ &\quad + \mu_0 \langle \mathbf{H}(\mathbf{r}, \omega) \otimes \mathbf{H}^*(\mathbf{r}, \omega') \rangle e^{-i(\omega - \omega')t} \\ &\quad - \frac{1}{2} \epsilon_0 \text{Tr} \left\{ \langle \mathbf{E}(\mathbf{r}, \omega) \otimes \mathbf{E}^*(\mathbf{r}, \omega') \rangle e^{-i(\omega - \omega')t} \right\} \mathbb{I} \\ &\quad - \frac{1}{2} \mu_0 \text{Tr} \left\{ \langle \mathbf{H}(\mathbf{r}, \omega) \otimes \mathbf{H}^*(\mathbf{r}, \omega') \rangle e^{-i(\omega - \omega')t} \right\} \mathbb{I}]. \end{aligned} \quad (13)$$

Using FDT from Eq. 10 and Eq. 11, the above expression can be reduced to the integration of the terms containing $\langle \mathbf{E}(\mathbf{r}, \omega) \otimes \mathbf{E}^*(\mathbf{r}, \omega) \rangle$ and $\langle \mathbf{H}(\mathbf{r}, \omega) \otimes \mathbf{H}^*(\mathbf{r}, \omega) \rangle$. As we discussed in the last section, Eq. 10 and Eq. 11 introduce two different sources that contribute to the total field correlations. The first one is the fluctuating particle dipoles determined by the temperatures of bodies. In the TDDA approach, it can be written as:

$$\langle \bar{\mathbf{P}}_f(\omega) \bar{\mathbf{P}}_f^\dagger(\omega') \rangle = 2\pi\hbar\epsilon_0\delta(\omega - \omega') [\mathbb{I} + 2\hat{n}_B(\omega, T_1, T_2)] \hat{\chi}, \quad (14)$$

where T_1 and T_2 are the temperatures of the two objects, and $\hat{n}_B(\omega, T_1, T_2)$ is a diagonal tensor with $3N$ elements given by the Bose-Einstein distribution. $\hat{\chi}$ is a tensor combining the imaginary part of the polarization tensor and the radiative correction [48, 49]. Using the general TDDA equations and some algebraic manipulations, we obtain the following expressions for the correlations of electric and magnetic fields at the observation point outside bodies:

$$\langle \mathbf{E}(\mathbf{r}, \omega) \otimes \mathbf{E}^*(\mathbf{r}, \omega) \rangle = \frac{k_0^4}{\epsilon_0^2} \mathbf{G}_{EE} \bar{\mathbf{T}}^{-1} \langle \bar{\mathbf{P}}_f \bar{\mathbf{P}}_f^\dagger \rangle \bar{\mathbf{T}}^{-1\dagger} \mathbf{G}_{EE}^\dagger, \quad (15)$$

$$\langle \mathbf{H}(\mathbf{r}, \omega) \otimes \mathbf{H}^*(\mathbf{r}, \omega) \rangle = \frac{k_0^4}{\epsilon_0^2} \mathbf{G}_{HE} \bar{\mathbf{T}}^{-1} \langle \bar{\mathbf{P}}_f \bar{\mathbf{P}}_f^\dagger \rangle \bar{\mathbf{T}}^{-1\dagger} \mathbf{G}_{HE}^\dagger \quad (16)$$

where $\mathbf{T}_{ij} = \delta_{ij}\mathbb{I} - (1 - \delta_{ij})k_0^2\bar{\alpha}_i\bar{\mathbf{G}}_{EE,ij}$ and \mathbf{G}_{HE} is the magnetic-electric field Green's tensor (Eq. A15). More details about the derivation are shown in Appendix A 1.

The second source is the environmental field fluctuation. The fluctuational electric fields in the vacuum can induce electric dipoles on the objects and then generate electromagnetic fields at the observation point. In this case, the field-field correlations at the observation point outside bodies are given by (Appendix A 2):

$$\begin{aligned} \langle \mathbf{E}(\mathbf{r}, \omega) \otimes \mathbf{E}^*(\mathbf{r}, \omega) \rangle &= k_0^4 \mathbf{G}_{EE} \bar{\mathbf{T}}^{-1} \bar{\alpha} \langle \bar{\mathbf{E}}_f \bar{\mathbf{E}}_f^\dagger \rangle \bar{\alpha}^\dagger \bar{\mathbf{T}}^{-1\dagger} \mathbf{G}_{EE}^\dagger \\ &\quad + k_0^2 \mathbf{G}_{EE} \bar{\mathbf{T}}^{-1} \bar{\alpha} \langle \bar{\mathbf{E}}_f \mathbf{E}_f^\dagger \rangle \\ &\quad + k_0^2 \langle \mathbf{E}_f \bar{\mathbf{E}}_f^\dagger \rangle \bar{\alpha}^\dagger \bar{\mathbf{T}}^{-1\dagger} \mathbf{G}_{EE}^\dagger, \end{aligned} \quad (17)$$

$$\begin{aligned} \langle \mathbf{H}(\mathbf{r}, \omega) \otimes \mathbf{H}^*(\mathbf{r}, \omega) \rangle &= k_0^4 \mathbf{G}_{HE} \bar{\mathbf{T}}^{-1} \bar{\alpha} \langle \bar{\mathbf{E}}_f \bar{\mathbf{E}}_f^\dagger \rangle \bar{\alpha}^\dagger \bar{\mathbf{T}}^{-1\dagger} \mathbf{G}_{HE}^\dagger \\ &\quad + k_0^2 \mathbf{G}_{HE} \bar{\mathbf{T}}^{-1} \bar{\alpha} \langle \bar{\mathbf{E}}_f \mathbf{H}_f^\dagger \rangle \\ &\quad + k_0^2 \langle \mathbf{H}_f \bar{\mathbf{E}}_f^\dagger \rangle \bar{\alpha}^\dagger \bar{\mathbf{T}}^{-1\dagger} \mathbf{G}_{HE}^\dagger. \end{aligned} \quad (18)$$

where

$$\langle \bar{\mathbf{E}}_f(\omega) \bar{\mathbf{E}}_f^\dagger(\omega') \rangle = 2\pi\hbar\epsilon_0\delta(\omega - \omega') (1 + 2n_0(\omega)) \text{Im} \bar{\mathbf{G}}_{EE}, \quad (19)$$

$$\langle \bar{\mathbf{E}}_f(\omega) \mathbf{E}_f^\dagger(\omega') \rangle = 2\pi\hbar\epsilon_0\delta(\omega - \omega') (1 + 2n_0(\omega)) \text{Im} \mathbf{G}_{EE}, \quad (20)$$

$$\langle \mathbf{H}_f(\omega) \bar{\mathbf{E}}_f^\dagger(\omega') \rangle = 2\pi\hbar\epsilon_0\delta(\omega - \omega') (1 + 2n_0(\omega)) \text{Im} \mathbf{G}_{HE}. \quad (21)$$

are the vacuum electric-electric field correlation inside bodies, the vacuum electric-electric field correlation between the object position and observation point, and the vacuum electric-magnetic field correlation between the object position and observation point, respectively. Generally, these two sources have opposite contributions to the total far field radiations and at global thermal equilibrium, they should cancel each other to satisfy the detailed balance of the radiative AM flux.

III. NUMERICAL RESULTS

In this section, we present the numerical results related to the radiative AM transfer and the induced torques discussed in the previous sections. In order to explore the role played by nonreciprocity, we consider the near-field and far-field radiation from single- and two-cube systems that are made of nonreciprocal materials. Here we choose doped InSb as an example. InSb is a MO material whose permittivity model has been well-characterized experimentally [50–53]. Subjected to an external magnetic field, it shows gyroelectric properties with gyrotropic axis along the magnetic field. The permittivity tensor in an arbitrary magnetic field takes the form

of $\bar{\epsilon} = \epsilon_\infty [1 + (\omega_L^2 - \omega_T^2) / (\omega_T^2 - \omega^2 - i\Gamma\omega)] \mathbb{I}_{3 \times 3} + \epsilon_\infty \omega_p^2 [\mathbb{I}_3 \times 3(\omega)]^{-1}$ [29], where

$$\mathbb{I}_{3 \times 3}(\omega) = \begin{bmatrix} -\omega^2 - i\gamma\omega & -i\omega\omega_{cz} & i\omega\omega_{cy} \\ i\omega\omega_{cz} & -\omega^2 - i\gamma\omega & -i\omega\omega_{cx} \\ -i\omega\omega_{cy} & i\omega\omega_{cx} & -\omega^2 - i\gamma\omega \end{bmatrix}.$$

Here, ϵ_∞ is the high-frequency dielectric constant, ω_L is the longitudinal optical-phonon frequency, ω_T is the transverse optical-phonon frequency, ω_p is the plasma frequency of the free carriers of density n . Γ is the phonon damping constant, and γ is the free-carrier damping constant. And ω_{ci} ($i=x,y,z$) is the cyclotron frequency given by $\omega_{ci} = qB_j/m_f$. All the parameters are taken from [51, 52], where doping density $n = 10^{17} \text{ cm}^{-3}$, $\epsilon_\infty = 15.7$, $\omega_L = 3.62 \times 10^{13} \text{ rad s}^{-1}$, $\omega_T = 3.39 \times 10^{13} \text{ rad s}^{-1}$, $\omega_p = 3.14 \times 10^{13} \text{ rad s}^{-1}$, $\Gamma = 5.65 \times 10^{11} \text{ rad s}^{-1}$, $\gamma = 3.39 \times 10^{12} \text{ rad s}^{-1}$, $m_f = 0.022m_e$ where $m_e = 9.1094 \times 10^{-31} \text{ kg}$ is electron mass.

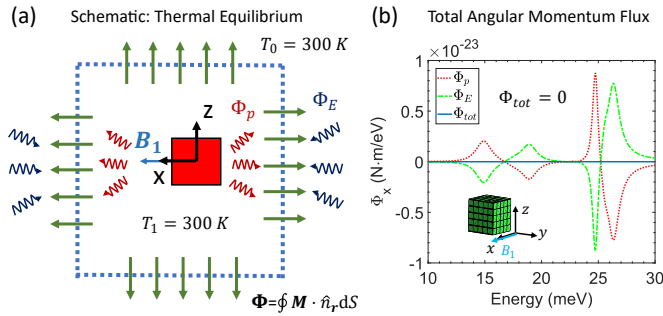


Figure 2. (Color online) (a) Schematic: Thermal radiation of the AM from a single InSb cube at thermal equilibrium ($T_1 = T_2 = 300 \text{ K}$). A 1 T external magnetic field along x direction is applied on the cube. A surface (blue dash line) that encloses the cube is chosen to compute the total AM flux (green arrows) radiated to the far field. (b) The spectrum of the total radiative AM flux at thermal equilibrium. The total flux (Φ_{tot}) is separated into two parts: one comes from the particle dipole fluctuations (denoted as Φ_p) and the other one originates from the environmental field fluctuations (denoted as Φ_E). At thermal equilibrium, Φ_p and Φ_E have the same magnitude but opposite signs, resulting in a zero total flux in the far field.

A. Thermal AM radiation from a single cube

As shown in figure 2(a) and 3(a), a single cube made of InSb is in the presence of an uniform magnetic field of 1 T along the x direction. The first issue we want to address now is the description of the thermal AM radiation from the single cube using the formalism detailed in Section II. Instead of using the SAM density $\mathbf{S}(\mathbf{r}) = \frac{\epsilon_0}{2\omega} \text{Im} \langle \mathbf{E}^*(\mathbf{r}) \times \mathbf{E}(\mathbf{r}) \rangle + \frac{\mu_0}{2\omega} \text{Im} \langle \mathbf{H}^*(\mathbf{r}) \times \mathbf{H}(\mathbf{r}) \rangle$ that has been utilized to quantify the spin component of the thermal radiation in our former work [29], here we define a tensor of angular-momentum flux density \mathbf{M} (Eq.

5) in analogy to the well-known Maxwell stress tensor. It allows us to compute the total flux Φ_{tot} of the radiative AM in the near-field and far-field, making a better connection between the thermal radiation and the induced torques. This definition includes the spin and orbital parts of the electromagnetic field. It reveals the whole story of the AM in the radiation and won't contradict the debate about the angular-momentum separation for electromagnetic fields [54–56].

Thermal equilibrium: We first consider a single cube in equilibrium with vacuum ($T_1 = T_0 = 300 \text{ K}$) and show the balance of the total AM flux Φ_{tot} in the far field (Fig. 2). To clarify the origin of the balance, we separate the total flux Φ_{tot} into two parts: $\Phi_{tot} = \Phi_p + \Phi_E$. Φ_p is induced by the fluctuational particle dipoles of the cube that is determined by the body temperature T_1 (Appendix A 1), while Φ_E comes from the environmental field fluctuations which is dependent on the environment temperature T_0 (Appendix A 2). Then we compute each AM flux Φ_i (for $i = x, y, z$) across the plane we defined. For this purpose, the AM flux is written as

$$\Phi_i = \int_A \langle M_{ji} \rangle dA_j, \quad (22)$$

which describes the integrated flux across a differential section dA perpendicular to the radial vector \mathbf{R} . Here we choose a surface that encloses the cube to compute the total AM flux radiated to the far field. As shown in Figure 2(b), the spectra of the thermal AM flux $\Phi_{x,p}$ and $\Phi_{x,E}$ have the same magnitude but opposite signs at each frequency. The total flux $\Phi_{x,tot}$ is zero as $\Phi_{x,p}$ and $\Phi_{x,E}$ perfectly cancel each other. The vanishing of $\Phi_{x,tot}$ satisfies the detailed balance of the AM flux and it indicates that there is no radiative torque applied on the cube at thermal equilibrium.

For Φ_y and Φ_z perpendicular to the gyrotropic axis, both of them are zero regardless of the temperatures and hence result in a zero total flux $\Phi_{i,tot}$ (for $i = y, z$). Since Φ_p and Φ_E have no contribution to the perpendicular component of the AM flux, the torques along y and z directions in this case will always remain zero no matter it is at thermal equilibrium or not. Thus, in our following discussions on the non-equilibrium case of a single cube, we only focus on the AM flux along the magnetic field (gyrotropic axis).

Thermal non-equilibrium: Here we show that thermal non-equilibrium can lead to a net radiative AM flux along the gyrotropic axis. As shown in Fig. 3 (a), We assume that the environment is at 0 K while the cube is kept at the room temperature $T_1 = 300 \text{ K}$. In this case, since the temperature of the cube is higher than the environment, Φ_p has a larger magnitude than Φ_E at each frequency and thus the summation of them gives a net AM flux along the magnetic field (Fig. 3(b)). Figure 3(d) and (e) depict the spatial distributions of the AM flux across yz-planes on the two sides of the cube. AM

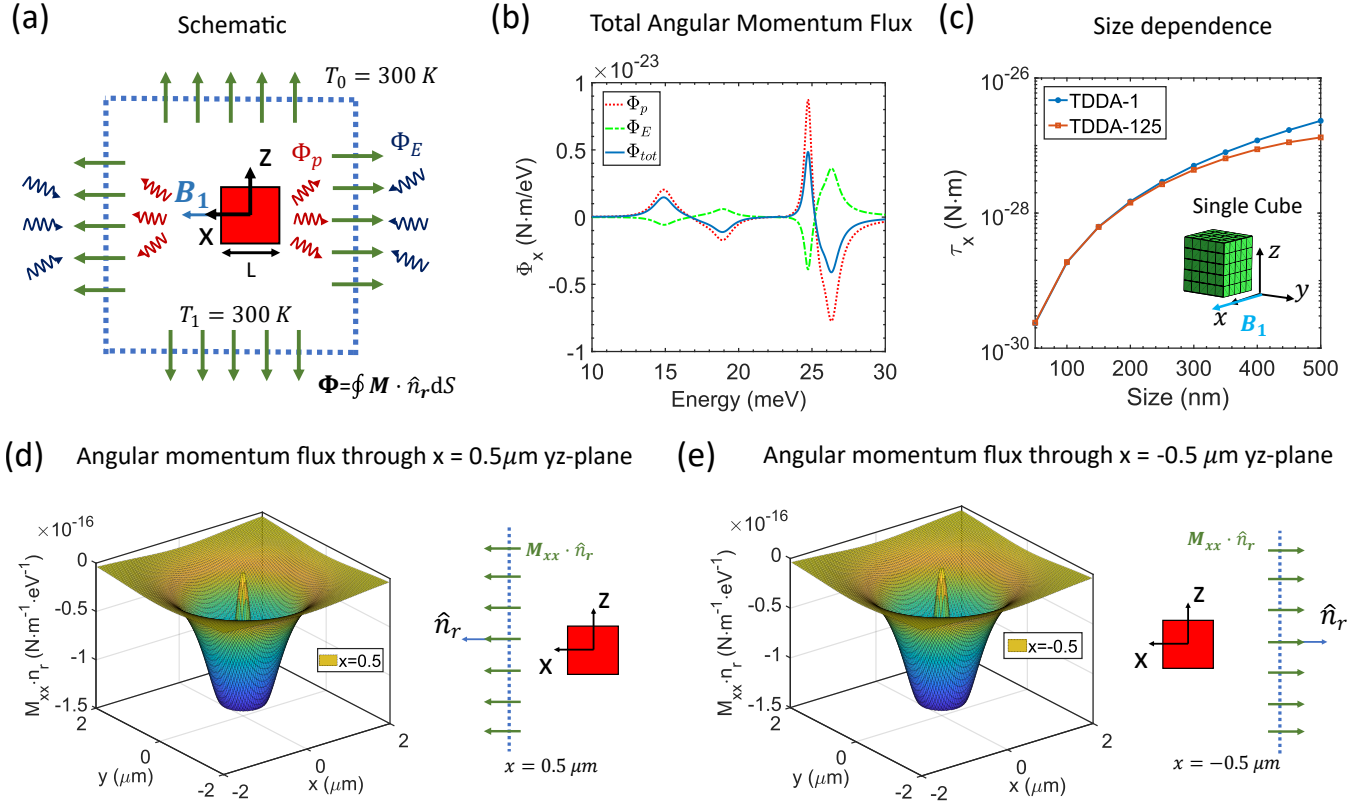


Figure 3. (Color online) Thermal radiation of the AM from a single InSb cube at thermal non-equilibrium. (a) Schematic: A cube is in presence of the magnetic field of 1 T along x direction. The cube is at 300 K while the environment is at 0 K. A surface that encloses the cube is chosen for computing the AM flux radiated to the far field. (b) Spectrum of Φ_x . At thermal non-equilibrium, Φ_p and Φ_E have unequal magnitudes and hence the total AM flux Φ_{tot} has a non-zero value. (c) Thermal non-equilibrium torque due to the AM radiation as a function of the cube size. The blue line with dot markers is computed by TDDA-1 (approximating the entire cube by a single dipole) and red line with square markers is obtained by using TDDA-125 (dividing each cube into 125 subvolumes and regarding each subvolume as a single dipole). (d) and (e) the spatial distribution of the AM flux through yz -planes at $x = 0.5\text{ }\mu\text{m}$ and $x = -0.5\text{ }\mu\text{m}$, respectively. Spatial distributions are plotted at the energy 0.2475 eV in thermal non-equilibrium case. The cube is assumed to be placed at origin.

flux at 24.75 meV is shown here as a typical example. The AM loss through the two planes (in front of and behind the cube) have an equal contribution to the total AM flux, giving a non-zero value of Φ_x . The other components that are perpendicular to the gyrotropic axis (Φ_y and Φ_z) still remain zero at thermal non-equilibrium. In total, a torque along the external magnetic fields is induced by the AM loss due to the thermal non-equilibrium between the cube and environment.

In Figure 3(c), we compute the thermal AM torque as a function of the cube size, and compare our numerical calculations to the dipole approximation. In TDDA-125, we divide each cube into 125 subvolumes, while for TDDA-1, we use a single point dipole to represent the object. At small sizes, the results from TDDA-1 and TDDA-125 show a good agreement. When the size of the cube increases, TDDA-125 gives a different magnitude as it takes the shape effect into consideration, which should be more precise than TDDA-1 for larger-size objects. Therefore, for following examples we will show next, we only focus

on the numerical results obtained by TDDA-125.

B. Thermal AM transfer in a two-cube system

In the previous section, we have shown that, for a single cube, there is no net AM flux going to the far field at thermal equilibrium. The non-vanishing AM flux along the gyroelectric axis only exists when the cube and the environment have different temperatures. However, things can be different for a two-body MO system. In a two-cube system, we find that a net AM flux can also exist at the near field between two cubes when the magnetic fields on each cube are misaligned. Such AM transfer induces an equilibrium torque between the cubes, which can be tuned by changing the angle between the magnetic fields.

Thermal equilibrium: In Fig. 4, the two-cube system is at global thermal equilibrium where $T_1 = T_2 = T_0 = 300\text{ K}$. T_1 , T_2 and T_0 denote the temperatures of the top cube, bottom cube and vacuum, respectively. To

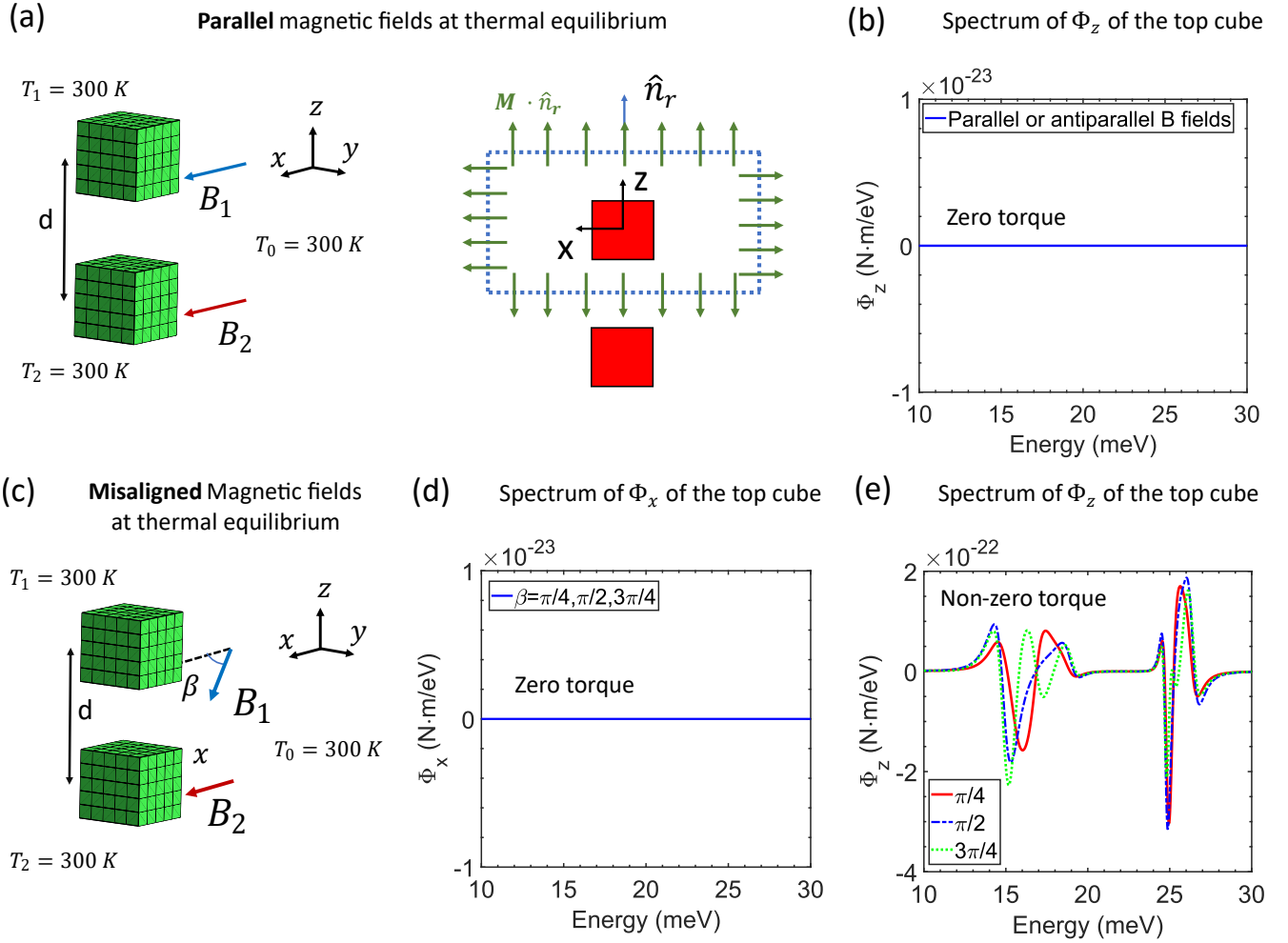


Figure 4. (Color online) Radiative AM transfer in a two-cube system at global thermal equilibrium ($T_1=T_2=T_0=300$ K). (a) Schematic: The parallel magnetic fields with the same magnitude $B_1=B_2=1$ T are applied on both cubes. The size of cubes is $L=500$ nm and they are separated by $d=1$ μ m (center to center distance). (b) The spectrum of the total AM flux Φ_z emitted out from the top cube. In parallel/anti-parallel magnetic fields, Φ_z is always zero at global thermal equilibrium. (c) Schematic: The magnetic fields applied on the two cubes have the same magnitude $B_1=B_2=1$ T but with an angle β between each other. The size of cubes is $L=500$ nm and they are separated by $d=1$ μ m (center distance). (d) and (e) Spectra of the total AM flux Φ_i (for $i = x, z$, respectively) radiated from the top cube. The spectra are plotted with different magnetic field directions β . In the misaligned magnetic fields, Φ_z has a non-zero value while Φ_x still remains zero.

compute the total AM flux radiated from the top cube, we choose a box enclosing the top cube and calculate the flux across the surface, $\mathbf{M} \cdot \hat{\mathbf{n}}_{\mathbf{r}}$. If the magnetic fields on two cubes are parallel (Fig. 4 (a)-(b)), there is no AM flux going out from each cube, which is similar to the single cube case. However, once the magnetic fields are misaligned, the gyrotropic axes of the cubes are along different directions (Fig 4 (c)-(e)). And then surprisingly, there is a net AM flux along z direction (perpendicular to the plane formed by the two gyrotropic axes) transferring between two cubes. Meanwhile, Φ_x and Φ_y still remain zero regardless of the angle β .

Such AM transfer of Φ_z is interesting but non-intuitive since it can occur despite the global thermal equilibrium. It is also important to point out that the presence of the non-zero radiative AM transfer at the global thermal

equilibrium does not lead to any thermodynamic contradictions. To demonstrate this argument, we separately compute the AM flux Φ_z across different xy -planes to reveal the origins of the transferring process (Fig. 5). Here, we typically choose three planes to show the flux Φ_z : (b) The mid plane between two cubes; (c) the top plane above the top cube; (d) the bottom plane below the bottom cube. The mid xy -plane shows the near field AM transfer between the cubes, while the top and bottom planes show the AM flux going to the far field from each cube, respectively. Here we do not show the AM flux leaking through the other surfaces since their contributions to Φ_z are negligible compared to xy -planes we showed above. From Fig. 5, it is easy to find that the AM flux Φ_z mainly transfers through the mid xy -plane, with almost two-order larger magnitude than the

top and bottom planes. Moreover, the fluxes Φ_z across the top and bottom planes have the same magnitude but different signs (directions) at each frequency. Therefore, considering the total flux radiated to the environment from the combined two-cube system, (c) and (d) cancel each other and give a zero net flux of Φ_z . This means that such AM transfer is a localized phenomenon and won't cause any net flux that transfers between the system and the surrounding environment, conserving AM globally.

With a net AM flux transferring between the cubes, an equilibrium torque is induced on each cube. Such equilibrium torque can be tuned by changing the angle between the magnetic fields and vanishes when the magnetic fields are parallel. Fig. 6 plots magnetic field dependence of the equilibrium torque. Here we assume that the magnetic field on the bottom cube is fixed while we change the angle β of the B field on the top cube. Similar to what we did in the last subsection, we separate the torques into two parts originating from the particle dipole fluctuations (M_p) and the environment field fluctuations (M_E), respectively.

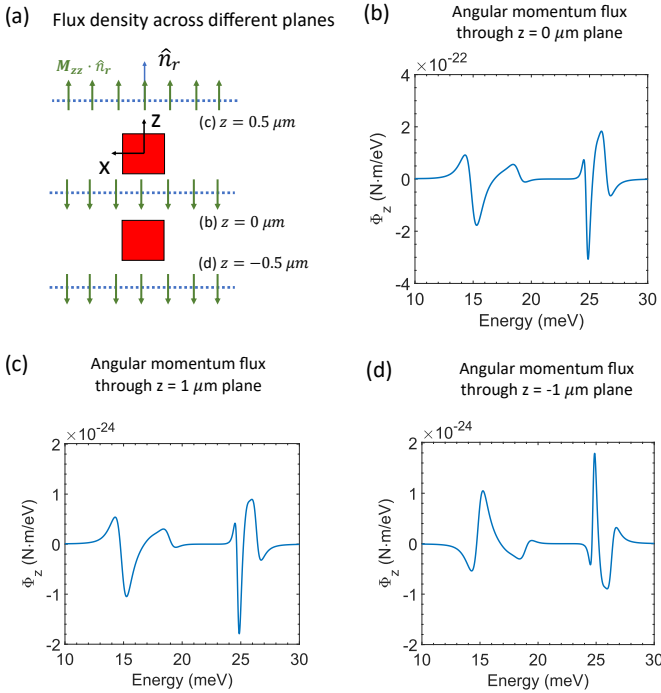


Figure 5. (Color online) Near-field AM flux in a two-cube system at global thermal equilibrium ($T_1=T_2=T_0=300$ K). The size of cubes is $L=500$ nm and they are separated by $d=1 \mu\text{m}$. The magnitudes of the external magnetic fields are $B_1=B_2=1$ T. (a) Schematic. (b)-(d) The spectra of AM flux Φ_z across three different xy-planes as shown in (a). Here β is assumed to be $\pi/2$. Figures (c) and (d) show the radiation flux to the environment, and they contribute oppositely to the total flux Φ_z of the combined two-cube system. At thermal equilibrium, (c) and (d) perfectly cancel each other, giving no net torque on the combined system.

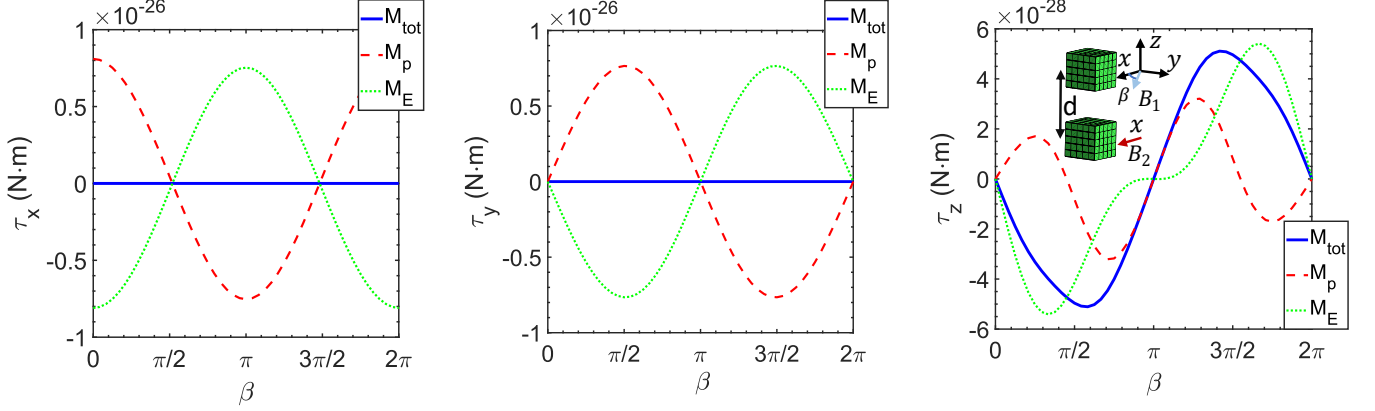
First we only consider the torques within the xy-plane where the magnetic fields are applied. In this case, M_p and M_E have the same magnitude but different signs and hence result in a zero net torque within the xy-plane on each cube. The vanishing of the torque in xy-planes is independent of β and is always true at global thermal equilibrium. Unlike the single-body system where the M_p and M_E should be exactly along its gyrotropic axis (magnetic field), here they can be slightly misaligned with their own gyrotropic axis. Such misalignment originates from the interaction between the cubes since M_p (M_E) of the bottom cube in a fixed magnetic field varies when we tune the direction of the B field on the top cube (the left two plots in Fig. 6 (b)). The torque that is perpendicular to the external magnetic field has a much smaller magnitude than the parallel component, indicating that the interaction is weak at global thermal equilibrium.

Along the z direction perpendicular to the plane formed by the magnetic fields, a torque is induced by the AM transfer between two cubes despite global thermal equilibrium (the right plots in Fig. 6). When the magnetic fields on two cubes are parallel or anti-parallel, there is no torque applied because the AM transfer is prohibited. Otherwise, each cube feels a torque along z direction trying to align their gyrotropic axes parallel to each other. Such torques have the same magnitude but opposite signs and, therefore, there is no net torque on the combined system, conserving the global AM at thermal equilibrium.

It is noted that, at thermal equilibrium, there are two distinct zero-torque configurations: parallel magnetic fields ($\beta = 0$) and anti-parallel magnetic fields ($\beta = \pi$). If the system starts from the anti-parallel configuration ($\beta = \pi$), two cubes have a tendency to relax back to the parallel configuration. It means that $\beta = \pi$ is an unstable equilibrium point that is sensitive to a tiny disturbance. On the other hand, if two cubes are left in the parallel configuration ($\beta = 0$), they will remain in it and tend to go back after a small disturbance.

Finally, we plot the temperature dependence and distance dependence of the torque τ_z in Figure 7. Temperature affects the AM flux through the mean thermal energy $\Theta(\omega, T) = \hbar\omega/2 + \hbar\omega/[\exp(\hbar\omega/k_B T) - 1]$. Since the mean thermal energy is approximately constant over the frequency range of interest, the magnitude of τ_z increases proportionately with the temperature. The left figure in Fig. 7(b) demonstrates the spectrum for Φ_z as a function of distance between two cubes. At each frequency, the sign (the direction of the radiative AM flux) keeps the same while the magnitude decays as a function of distance. The right figure in Fig. 7(b) shows the torque along z direction after doing integral of Φ_z over frequency. Similarly, the magnitude of the torque τ_z decreases as a function of distance while keeps the direction unchanged. It confirms that the radiative AM transfer for Φ_z at global thermal equilibrium originates from the near-field interaction between the cubes, as the interaction strength is strongly determined by the distance.

(a) Torques on the top cube



(b) Torques on the bottom cube

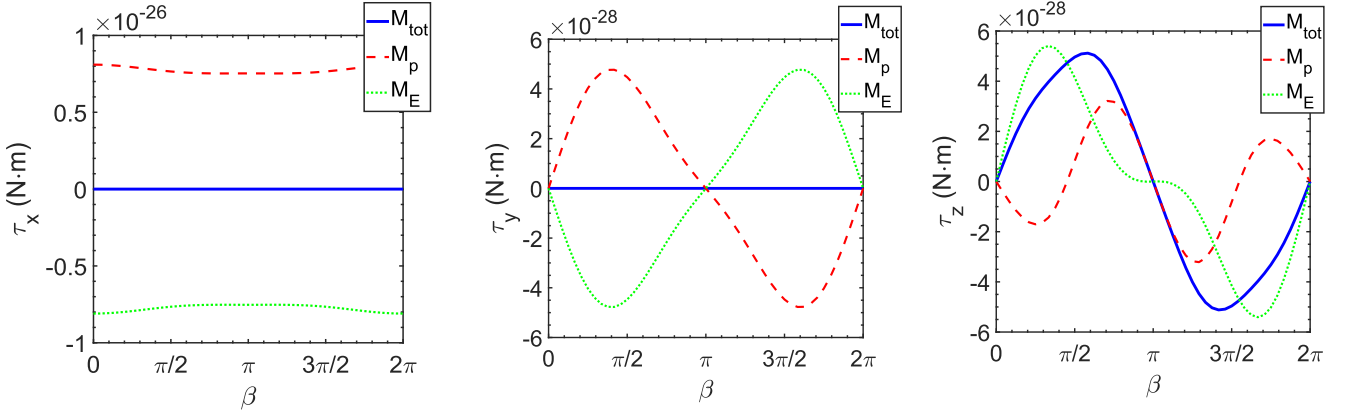


Figure 6. (Color online) Torques induced by radiative AM transfer at global thermal equilibrium ($T_1 = T_2 = T_0 = 300$ K) as functions of magnetic field angle β . The total torque on each cube are separated into two parts according to their origins: M_p is induced by fluctuational dipoles and M_E comes from field fluctuations. M_{tot} is the total torque on each cube that combines M_p and M_E . Other parameters are $L=500$ nm, $B_1=B_2=1$ T, $d=1$ μm . (a) Torques on the top cube in a varied magnetic field. (b) Torques on the bottom cube in a fixed magnetic field along x axis.

Thermal non-equilibrium: Above we have shown that, for a two-cube system at global thermal equilibrium ($T_1 = T_2 = T_0$), AM transfer can only happen along z direction. And we have also pointed out that there is no torque within xy-plane at global thermal equilibrium due to the balance between M_p and M_E , which are slightly misaligned with their gyrotropic axes. Here we are going to show that non-equilibrium ($T_1 \neq T_2$) helps amplify the interaction between the cubes, making the AM transfer between two cubes much stronger than the equilibrium case.

Figure 8 depicts magnetic field dependence of the radiative AM torques at thermal non-equilibrium. As shown in Figure 8 (a), we assume that the top cube is heated up to $T_1 = 500$ K, while the bottom cube keeps in equilibrium with the environment ($T_2 = T_0 = 300$ K). Similarly, we tune the direction of the magnetic field on the top cube and compute the non-equilibrium torque as a function of β . In this case, the torques on each cube

are strongly modified due to the near-field AM transfer (Figure 8 (b)-(d)). First, the torques within the xy-plane no longer follows the direction of the external magnetic fields. On the contrary, the torques in the xy-plane have a big departure from the gyrotropic axes. Second, the torque in xy-plane on bottom cube (in a fixed magnetic field) also shows a strong dependence of the magnetic field B_1 applied on the top cube. At each angle β , the torques on two cubes have comparable magnitudes and opposite signs. Their summation gives a smaller total torque on the combined system, which is one order smaller than the torque on each cube. Third, the torques along z direction are amplified by two orders than the equilibrium case, directly indicating that the radiative AM transfer is strongly amplified because of the unequal temperatures of two cubes.

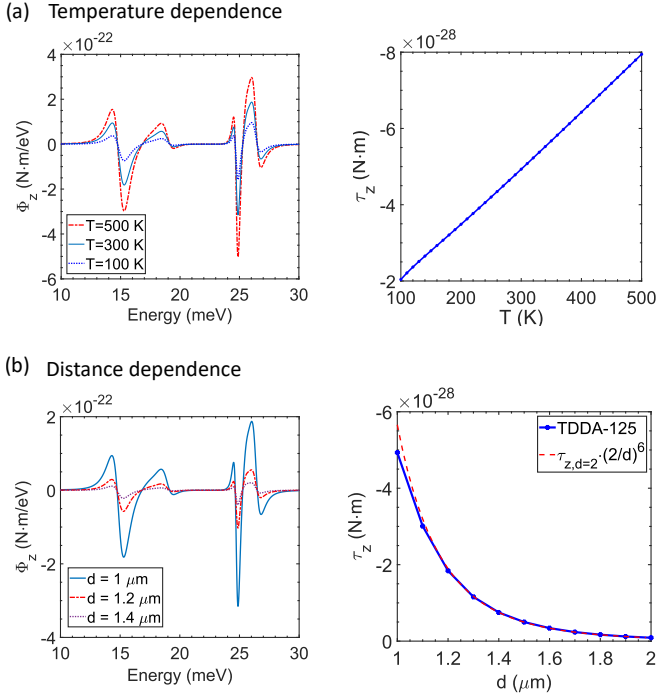


Figure 7. (Color online) (a) Temperature dependence of the near-field AM flux Φ_z across the mid xy-plane between two cubes. The system remains at global thermal equilibrium $T_1 = T_2 = T_0$ while tuning the temperature. Here we assume that $\beta = \pi/2$, $d = 1 \mu\text{m}$ and $L = 500$ nm. (Left figure) Spectra of Φ with different temperatures. (Right figure) Induced torque as a function of temperature. (b) Distance dependence of the near-field AM flux Φ_z that goes through the mid xy-plane between two cubes. The red dash line is plotted by multiplying the torque at $d=2 \mu\text{m}$ and $(2/d)^6$, which is the ratio to the power of 6 between the torques at two distances. Parameters are $T_1 = T_2 = T_0 = 300$ K, $\beta = \pi/2$, $d = 1 \mu\text{m}$ and $L = 500$ nm. (Left figure) Spectra of Φ_z at different distances. (Right figure) The equilibrium torque τ_z as a function of distance.

IV. ADDITIONAL REMARKS AND CONCLUSIONS

We explored a different perspective of AM-resolved thermal radiation and demonstrate radiative AM related phenomena in non-reciprocal systems. We have developed the TDDA approach based on fluctuational electrodynamics for analyzing the thermal AM flux density at the near-field and far-field of finite non-reciprocal bodies. Our work reveals that the AM loss due to far-field radiation plays a fundamental role in generating a thermal AM torque along the gyroelectric axis of a single non-reciprocal body at thermal non-equilibrium. The connection between the thermal radiation of nonreciprocal bodies and the induced torques is important for exploring new ways of directional thermal AM transfer.

We also found that in a two-body nonreciprocal system, the thermal AM can also transfer at the near field between two objects. This is a localized phenomenon

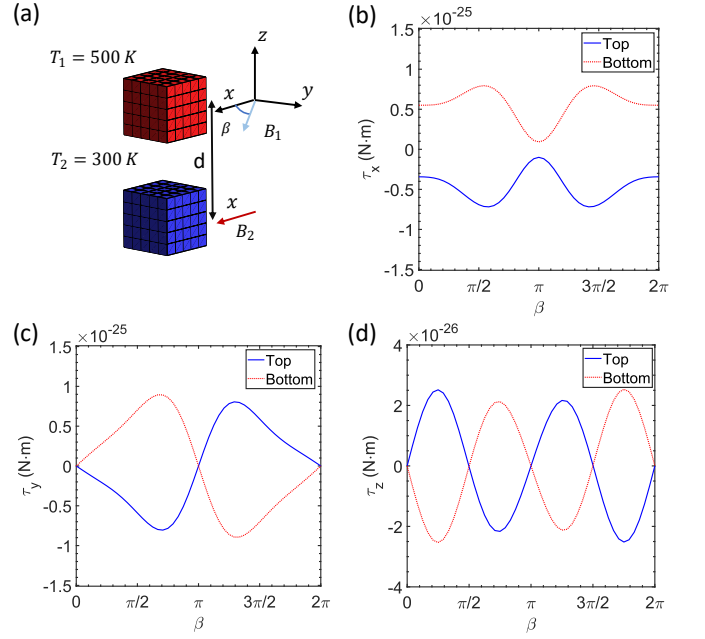


Figure 8. (Color online) Thermal non-equilibrium torques when the top cube is heated up to $T_1=500$ K and the bottom cube still remains thermal equilibrium with surroundings, $T_2 = T_0 = 300$ K. The size of cubes is $L = 500$ nm and they are separated by $d = 1 \mu\text{m}$. (a) Schematic of the thermal non-equilibrium case. (b)-(d) Torques as functions of direction of the magnetic field. The magnetic field on the bottom cube is fixed, while the direction of the magnetic field on the top cube is varied from 0 to 2π .

that only happens as the near-field interaction between two bodies and decays fast with the increasing body distance. Also, such near-field interaction won't contribute to any net radiative AM flux at far field for the combined system. Moreover, the near-field AM flux across the plane between two bodies is not necessary to be always along their gyroelectric axes. With misaligned gyroelectric axes, an AM perpendicular to the plane formed by two gyroelectric axes can transfer between two bodies despite global thermal equilibrium. It induces torques on both cubes trying to align two gyroelectric axes parallel to each other. At global thermal equilibrium, the torques on two cubes have the same magnitude but opposite signs, and the net torque on the combined system is zero, satisfying the detailed balance of AM exchange between the combined system and the environment at equilibrium.

Some recent works predicted that the torques can be induced by vacuum friction of a rotating object made of reciprocal isotropic media [57–60]. These predictions are of good interest in the context of nanophotonics [16, 61–67] and Casimir physics [14, 68–70], as they are fundamentally originated from quantum and thermal fluctuations. However, such rotational vacuum frictions still remain at the theoretical level and, so far, no experimental observation has been done due to the extremely small magnitudes of the torques which are far below the sen-

sitivity that can be achieved by the torque sensor [71]. Many theoretical works tried to enhance the vacuum friction to make it more measurable than a single rotating particle [57], such as using surface plasmon resonance [58] and surface photon tunneling [60]. Recently, an experimental demonstration of the most sensitive torque measurement has been done with levitated nanoparticle, improving the torque sensitivity by a few orders [63] and showing the feasibility for detecting the rotational vacuum friction near a surface. As we have shown in this work, the thermal AM torque in a MO system in the presence of external magnetic fields has a comparable magnitude with the sensitivity that can be achieved by the levitated torque sensor [63] and it is tunable by changing the external magnetic fields. Therefore, the thermal AM torques in the MO system are possible to be experimentally detected in the near future.

Finally, the TDDA approach we have developed in this work can be applied to describe the radiative AM transfer of finite objects with arbitrary size and shape. This formalism allows us to compute the radiative AM flux at the near-field as well as far-field of the MO bodies with arbitrary permittivity tensors. We have used this TDDA approach to explore how the nonreciprocity affects the radiation of AM in single-cube and two-cube systems. Our work provides a way for describing AM-resolved thermal radiation involving finite MO bodies of arbitrary shape.

ACKNOWLEDGMENTS

We are grateful to the supports from the DARPA QUEST program and the Office of Naval Research under Grant No. N00014-18-1-2371.

Appendix A: TDDA Approach to Radiative AM Flux

In this section, we develop a TDDA method for calculating the AM flux density based on the former works [36–38]. Here we separate the discussion into two parts: particle dipole fluctuations and environmental field fluctuations. These two contributions correspond to the emission of objects and the absorption from surrounding environment, respectively. And they will be balanced when the system is in equilibrium with the environment.

In particular, here we consider the case of two finite objects assumed to be at fixed temperatures T_1 and T_2 and they both interact with a thermal bath at temperature T_0 . We assume that these two objects are described by a collection of N_p (for object p) electric point dipoles. Each dipole is characterized by a volume $V_{i,p}$ and a polarizability tensor $\hat{\alpha}_{i,p}$, where $p=1,2$ denotes the body that the dipole belongs to and $i=1,2,\dots,N_p$ indicates the i -th subvolume in that object. We group the electric dipoles

and electric fields in a compact form

$$\begin{aligned} \bar{\mathbf{P}} &= \begin{pmatrix} \bar{\mathbf{P}}_1 \\ \bar{\mathbf{P}}_2 \end{pmatrix}; \quad \bar{\mathbf{P}}_1 = \begin{pmatrix} \mathbf{P}_{1,1} \\ \vdots \\ \mathbf{P}_{N_1,1} \end{pmatrix}, \bar{\mathbf{P}}_2 = \begin{pmatrix} \mathbf{P}_{1,2} \\ \vdots \\ \mathbf{P}_{N_2,2} \end{pmatrix} \\ \bar{\mathbf{E}} &= \begin{pmatrix} \bar{\mathbf{E}}_1 \\ \bar{\mathbf{E}}_2 \end{pmatrix}; \quad \bar{\mathbf{E}}_1 = \begin{pmatrix} \mathbf{E}_{1,1} \\ \vdots \\ \mathbf{E}_{N_1,1} \end{pmatrix}, \bar{\mathbf{E}}_2 = \begin{pmatrix} \mathbf{E}_{1,2} \\ \vdots \\ \mathbf{E}_{N_2,2} \end{pmatrix} \end{aligned} \quad (\text{A1})$$

Then we can define the polarizability tensor as $\bar{\alpha} = \begin{pmatrix} \bar{\alpha}_1 & 0 \\ 0 & \bar{\alpha}_2 \end{pmatrix}$ and $\bar{\alpha}_p = \text{diag}(\hat{\alpha}_{1,p}, \dots, \hat{\alpha}_{N_p,p})$, ($p=1,2$). And each element $\hat{\alpha}_{i,p}$ is given by [38]

$$\hat{\alpha}_{i,p} = \left(\frac{1}{V_p} \left(\hat{L}_p + [\hat{\epsilon}_p - \mathbb{I}]^{-1} \right) - i \frac{k_0^3}{6\pi} \mathbb{I} \right)^{-1} \quad (\text{A2})$$

where $\hat{\epsilon}_p$ is the dielectric permittivity tensor, V_p is the volume of each discrete dipole, and \hat{L}_p is the depolarization tensor which is $\hat{L}_p = (1/3)\mathbb{I}$ for cubic volume mesh element [38, 72, 73].

To compute the total radiative momentum and AM flux that are described in terms of the surface integral of the flux densities as Eq. (3) and Eq. (7), we need to compute the statistical average of the momentum and AM flux density by Eq. (2) and Eq. (5). For ease of analysis, the average is expressed in terms of the Fourier transforms

$$\begin{aligned} \langle \Sigma(\mathbf{r}) \rangle &= -2 \int_0^\infty \frac{d\omega}{2\pi} \int_{-\infty}^\infty \frac{d\omega'}{2\pi} \\ &\quad \text{Re}[\epsilon_0 \langle \mathbf{E}(\mathbf{r}, \omega) \otimes \mathbf{E}^*(\mathbf{r}, \omega') \rangle e^{-i(\omega-\omega')t} \\ &\quad + \mu_0 \langle \mathbf{H}(\mathbf{r}, \omega) \otimes \mathbf{H}^*(\mathbf{r}, \omega') \rangle e^{-i(\omega-\omega')t} \\ &\quad - \frac{1}{2} \epsilon_0 \text{Tr} \left\{ \langle \mathbf{E}(\mathbf{r}, \omega) \otimes \mathbf{E}^*(\mathbf{r}, \omega') \rangle e^{-i(\omega-\omega')t} \right\} \mathbb{I} \\ &\quad - \frac{1}{2} \mu_0 \text{Tr} \left\{ \langle \mathbf{H}(\mathbf{r}, \omega) \otimes \mathbf{H}^*(\mathbf{r}, \omega') \rangle e^{-i(\omega-\omega')t} \right\} \mathbb{I}] \end{aligned} \quad (\text{A3})$$

for momentum flux density and

$$\begin{aligned} \langle \mathbf{M}(\mathbf{r}) \rangle &= -2 \int_0^\infty \frac{d\omega}{2\pi} \int_{-\infty}^\infty \frac{d\omega'}{2\pi} \mathbf{r} \times \\ &\quad \text{Re}[\epsilon_0 \langle \mathbf{E}(\mathbf{r}, \omega) \otimes \mathbf{E}^*(\mathbf{r}, \omega') \rangle e^{-i(\omega-\omega')t} \\ &\quad + \mu_0 \langle \mathbf{H}(\mathbf{r}, \omega) \otimes \mathbf{H}^*(\mathbf{r}, \omega') \rangle e^{-i(\omega-\omega')t} \\ &\quad - \frac{1}{2} \epsilon_0 \text{Tr} \left\{ \langle \mathbf{E}(\mathbf{r}, \omega) \otimes \mathbf{E}^*(\mathbf{r}, \omega') \rangle e^{-i(\omega-\omega')t} \right\} \mathbb{I} \\ &\quad - \frac{1}{2} \mu_0 \text{Tr} \left\{ \langle \mathbf{H}(\mathbf{r}, \omega) \otimes \mathbf{H}^*(\mathbf{r}, \omega') \rangle e^{-i(\omega-\omega')t} \right\} \mathbb{I}] \end{aligned} \quad (\text{A4})$$

for AM flux density. Here we have used the properties that $\mathbf{E}(\mathbf{r}, -\omega) = \mathbf{E}(\mathbf{r}, \omega)^*$ and $\mathbf{H}(\mathbf{r}, -\omega) = \mathbf{H}(\mathbf{r}, \omega)^*$. Using FDT from Eq. 10 and Eq. 11, the above expression can be reduced to the integration of the terms containing $\langle \mathbf{E}(\mathbf{r}, \omega) \otimes \mathbf{E}^*(\mathbf{r}, \omega) \rangle$ and $\langle \mathbf{H}(\mathbf{r}, \omega) \otimes \mathbf{H}^*(\mathbf{r}, \omega) \rangle$. In most cases of the remaining discussions, we drop the argument

ω to alleviate the notation. In the next two subsections, we will separately formalize the TDDA approach for computing the AM flux due to the electric dipole fluctuations and the electromagnetic field fluctuations.

1. Electric Dipole Fluctuation

We start by decomposing the local field $\mathbf{E}(\mathbf{r})$ outside the objects into the source field $\mathbf{E}_0(\mathbf{r})$ and the induced part $\mathbf{E}^{ind}(\mathbf{r})$:

$$\mathbf{E}(\mathbf{r}) = \mathbf{E}_0(\mathbf{r}) + \mathbf{E}^{ind}(\mathbf{r}). \quad (\text{A5})$$

The source field $\mathbf{E}_0(\mathbf{r})$ originates from the fluctuating dipole inside the objects and is given by

$$\mathbf{E}_0(\mathbf{r}) = \frac{k_0^2}{\epsilon_0} \mathbf{G}_{EE} \bar{\mathbf{P}}_f, \quad (\text{A6})$$

where $\mathbf{G}_{EE} = (\hat{G}_{EE}(\mathbf{r}, \mathbf{r}_1), \dots, \hat{G}_{EE}(\mathbf{r}, \mathbf{r}_N))$ is the row vector of the free-space Green tensors:

$$\hat{G}_{EE}(\mathbf{r}, \mathbf{r}') = \frac{e^{ik_0 R}}{4\pi R} \left[\left(1 + \frac{ik_0 R - 1}{k_0^2 R^2} \right) \hat{\mathbf{I}} + \left(\frac{3 - 3ik_0 R - k_0^2 R^2}{k_0^2 R^2} \right) \frac{\mathbf{R} \otimes \mathbf{R}}{R^2} \right] \quad (\text{A7})$$

where $\mathbf{R} = \mathbf{r} - \mathbf{r}'$ and $R = |\mathbf{r} - \mathbf{r}'|$. \otimes denotes the outer product of two vectors. The dyadic Green's tensor connects the fluctuating dipoles to the observation point outside the objects. $\bar{\mathbf{P}}_f$ is the fluctuating dipoles inside the objects and can be obtained by FDT

$$\langle \bar{\mathbf{P}}_f(\omega) \bar{\mathbf{P}}_f^\dagger(\omega') \rangle = 2\pi\hbar\epsilon_0\delta(\omega - \omega') [\mathbb{I} + 2\hat{n}_B(\omega, T_1, T_2)] \hat{\chi} \quad (\text{A8})$$

where $\hat{n}_B(\omega, T_1, T_2)$ is a diagonal tensor with $3N$ elements given by the Bose-Einstein distribution

$$\hat{n}_B(\omega, T_1, T_2) = \begin{pmatrix} n_1(\omega) \mathbb{I}_{3N_1 \times 3N_1} & \hat{\mathbf{0}} \\ \hat{\mathbf{0}} & n_2(\omega) \mathbb{I}_{3N_2 \times 3N_2} \end{pmatrix}. \quad (\text{A9})$$

and we have also introduced

$$\hat{\chi} = \frac{1}{2i} (\hat{\alpha} - \hat{\alpha}^\dagger) - \frac{k_0^3}{6\pi} \hat{\alpha}^\dagger \hat{\alpha}. \quad (\text{A10})$$

as the radiative correction [48, 49].

The second term in Eq. (A5) originates from the induced dipoles: $\mathbf{E}^{ind}(\mathbf{r}) = \frac{k_0^2}{\epsilon_0} \mathbf{G}_{EE} \bar{\mathbf{P}}^{ind}$. And the induced dipole $\bar{\mathbf{P}}^{ind}$ comes from the electric field inside the bodies as $\bar{\mathbf{P}}^{ind} = \epsilon_0 \bar{\alpha} \bar{\mathbf{E}}$, while $\bar{\mathbf{E}}$ can be obtained by solving TDDA equation

$$\bar{\mathbf{E}} = \bar{\mathbf{E}}_0 + k_0^2 d \bar{\mathbf{G}}_{EE} \bar{\alpha} \bar{\mathbf{E}}. \quad (\text{A11})$$

where $d\bar{\mathbf{G}}_{EE} = \bar{\mathbf{G}}_{EE} - \text{diag}\{\bar{\mathbf{G}}_{EE}\}$ and $\bar{\mathbf{G}}_{EE}$ is the matrix of the dyadic Green's tensors inside bodies that is also

defined by Eq. (A7). Here the overhead bar notation " - " indicates that the quantities are evaluated inside the bodies and it will be the same for other quantities in the following discussion. Solving Eq. (A11), we get the induced electric field

$$\mathbf{E}^{ind}(\mathbf{r}) = \frac{k_0^2}{\epsilon_0} \mathbf{G}_{EE} \bar{\mathbf{T}}^{-1} \bar{\mathbf{P}}_f \quad (\text{A12})$$

where

$$\mathbf{T}_{ij} = \delta_{ij} \mathbb{I} - (1 - \delta_{ij}) k_0^2 \bar{\alpha}_i \bar{\mathbf{G}}_{EE, ij} \quad (\text{A13})$$

Now, making use of Eq. (A13), we can compute the electric field correlation $\langle \mathbf{E}(\mathbf{r}, \omega) \otimes \mathbf{E}^*(\mathbf{r}, \omega) \rangle$ which is required for obtaining AM flux:

$$\langle \mathbf{E}(\mathbf{r}, \omega) \otimes \mathbf{E}^*(\mathbf{r}, \omega) \rangle = \frac{k_0^4}{\epsilon_0^2} \mathbf{G}_{EE} \bar{\mathbf{T}}^{-1} \langle \bar{\mathbf{P}}_f \bar{\mathbf{P}}_f^\dagger \rangle \bar{\mathbf{T}}^{-1\dagger} \mathbf{G}_{EE}^\dagger \quad (\text{A14})$$

Similarly, the magnetic field correlation $\langle \mathbf{H}(\mathbf{r}, \omega) \otimes \mathbf{H}^*(\mathbf{r}, \omega) \rangle$ can be obtained by replacing the electric-electric dyadic Green's tensor by the magnetic-electric Green's tensor:

$$\hat{G}_{HE}(\mathbf{r}, \mathbf{r}') = \frac{e^{ik_0 R}}{4\pi R} \left(1 + \frac{i}{k_0 R} \right) \sqrt{\frac{\epsilon_0}{\mu_0}} \begin{bmatrix} 0 & -\hat{\mathbf{r}}_z & \hat{\mathbf{r}}_y \\ \hat{\mathbf{r}}_z & 0 & -\hat{\mathbf{r}}_x \\ -\hat{\mathbf{r}}_y & \hat{\mathbf{r}}_x & 0 \end{bmatrix} \quad (\text{A15})$$

where $\hat{\mathbf{r}} = \mathbf{R}/R$, ($i = x, y, z$). Then we have

$$\langle \mathbf{H}(\mathbf{r}, \omega) \otimes \mathbf{H}^*(\mathbf{r}, \omega) \rangle = \frac{k_0^4}{\epsilon_0^2} \mathbf{G}_{HE} \bar{\mathbf{T}}^{-1} \langle \bar{\mathbf{P}}_f \bar{\mathbf{P}}_f^\dagger \rangle \bar{\mathbf{T}}^{-1\dagger} \mathbf{G}_{HE}^\dagger \quad (\text{A16})$$

2. Electromagnetic Field Fluctuation

Considering the interaction with the thermal bath, the fluctuating electromagnetic field will lead to the AM transfer and, to some extent, balances the contribution from the electric dipole fluctuation. The fluctuating electromagnetic field also fulfills the FDT which gives:

$$\langle \bar{\mathbf{E}}_f(\omega) \bar{\mathbf{E}}_f^\dagger(\omega') \rangle = 2\pi\hbar\epsilon_0\delta(\omega - \omega') (1 + 2n_0(\omega)) \text{Im} \bar{\mathbf{G}}_{EE} \quad (\text{A17})$$

$$\langle \bar{\mathbf{E}}_f(\omega) \mathbf{E}_f^\dagger(\omega') \rangle = 2\pi\hbar\epsilon_0\delta(\omega - \omega') (1 + 2n_0(\omega)) \text{Im} \mathbf{G}_{EE} \quad (\text{A18})$$

$$\langle \mathbf{H}_f(\omega) \bar{\mathbf{E}}_f^\dagger(\omega') \rangle = 2\pi\hbar\epsilon_0\delta(\omega - \omega') (1 + 2n_0(\omega)) \text{Im} \mathbf{G}_{HE} \quad (\text{A19})$$

It is noted that here we also considered the correlation between fluctuating fields inside bodies and at observation point outside bodies by Eq. (A18) and Eq. (A19). That is because the induced electric dipoles generate electric/magnetic field at the observation point that correlates to the local fluctuating field. However, we have ignored the correlation between fluctuating magnetic fields

due to the unit permeability ($\mu = 1$) of the media we are studying.

As usual, we decompose the local electric field at observation point into the source field and the induced field

$$\mathbf{E}(\mathbf{r}) = \mathbf{E}_0(\mathbf{r}) + \mathbf{E}^{ind}(\mathbf{r}). \quad (\text{A20})$$

And the source field \mathbf{E}_0 in this case is the bosonic field of the thermal bath so that $\mathbf{E}_0 = \mathbf{E}_f$. And the second term is the induced electric field from the induced dipoles $\mathbf{E}^{ind}(\mathbf{r}) = \frac{k_0^2}{\epsilon_0} \mathbf{G}_{EE} \bar{\mathbf{P}}^{ind}$. The induced dipole $\bar{\mathbf{P}}^{ind}$ in this case can be obtained by solving the TDDA equation for electric dipole

$$\bar{\mathbf{P}}^{ind} = \bar{\mathbf{P}}_0 + k_0^2 \bar{\alpha} d \bar{\mathbf{G}}_{EE} \bar{\mathbf{P}}^{ind} \quad (\text{A21})$$

where $\bar{\mathbf{P}}_0 = \epsilon_0 \bar{\alpha} \bar{\mathbf{E}}_f$ is directly induced by the local fluctuating field. Then we write the total electric field $\mathbf{E}(\mathbf{r})$ as

$$\mathbf{E} = \mathbf{E}_f + k_0^2 \bar{\alpha} \mathbf{G}_{EE} T^{-1} \bar{\alpha} \bar{\mathbf{E}}_f. \quad (\text{A22})$$

The first term \mathbf{E}_f on the left hand side (LHS) denotes the local fluctuating field at the observation point. $\bar{\mathbf{E}}_f$ in the second term of LHS is the fluctuating field inside bodies. The correlation of electric field at observation point is obtained with the help of Eq. (A22):

$$\begin{aligned} \langle \mathbf{E}(\mathbf{r}, \omega) \otimes \mathbf{E}^*(\mathbf{r}, \omega) \rangle = & k_0^4 \mathbf{G}_{EE} \bar{\mathbf{T}}^{-1} \bar{\alpha} \langle \bar{\mathbf{E}}_f \bar{\mathbf{E}}_f^\dagger \rangle \bar{\alpha}^\dagger \bar{\mathbf{T}}^{-1\dagger} \mathbf{G}_{EE}^\dagger \\ & + k_0^2 \mathbf{G}_{EE} \bar{\mathbf{T}}^{-1} \bar{\alpha} \langle \bar{\mathbf{E}}_f \mathbf{E}_f^\dagger \rangle \\ & + k_0^2 \langle \mathbf{E}_f \bar{\mathbf{E}}_f^\dagger \rangle \bar{\alpha}^\dagger \bar{\mathbf{T}}^{-1\dagger} \mathbf{G}_{EE}^\dagger \end{aligned} \quad (\text{A23})$$

Similarly, replacing \mathbf{G}_{EE} with \mathbf{G}_{HE} , we can get the correlation of magnetic field

$$\begin{aligned} \langle \mathbf{H}(\mathbf{r}, \omega) \otimes \mathbf{H}^*(\mathbf{r}, \omega) \rangle = & k_0^4 \mathbf{G}_{HE} \bar{\mathbf{T}}^{-1} \bar{\alpha} \langle \bar{\mathbf{E}}_f \bar{\mathbf{E}}_f^\dagger \rangle \bar{\alpha}^\dagger \bar{\mathbf{T}}^{-1\dagger} \mathbf{G}_{HE}^\dagger \\ & + k_0^2 \mathbf{G}_{HE} \bar{\mathbf{T}}^{-1} \bar{\alpha} \langle \bar{\mathbf{E}}_f \mathbf{H}_f^\dagger \rangle \\ & + k_0^2 \langle \mathbf{H}_f \bar{\mathbf{E}}_f^\dagger \rangle \bar{\alpha}^\dagger \bar{\mathbf{T}}^{-1\dagger} \mathbf{G}_{HE}^\dagger \end{aligned} \quad (\text{A24})$$

Now, combining Eq. (A4), (A14), (A16), (A23) and (A24), we can compute the total AM flux through arbitrary observation planes.

-
- [1] M. P. Bernardi, O. Dupré, E. Blandre, P.-O. Chapuis, R. Vaillon, and M. Francoeur, Impacts of propagating, frustrated and surface modes on radiative, electrical and thermal losses in nanoscale-gap thermophotovoltaic power generators, *Scientific reports* **5**, 1 (2015).
 - [2] E. Tervo, E. Bagherisereshki, and Z. Zhang, Near-field radiative thermoelectric energy converters: a review, *Frontiers in Energy* **12**, 5 (2018).
 - [3] P. J. Van Zwol, L. Ranno, and J. Chevrier, Tuning near field radiative heat flux through surface excitations with a metal insulator transition, *Physical review letters* **108**, 234301 (2012).
 - [4] A. Ghanekar, J. Ji, and Y. Zheng, High-rectification near-field thermal diode using phase change periodic nanostructure, *Applied Physics Letters* **109**, 123106 (2016).
 - [5] A. Babuty, K. Joulain, P.-O. Chapuis, J.-J. Greffet, and Y. De Wilde, Blackbody spectrum revisited in the near field, *Physical Review Letters* **110**, 146103 (2013).
 - [6] B. T. O'Callahan, W. E. Lewis, A. C. Jones, and M. B. Raschke, Spectral frustration and spatial coherence in thermal near-field spectroscopy, *Physical Review B* **89**, 245446 (2014).
 - [7] Y. Guo, C. L. Cortes, S. Molesky, and Z. Jacob, Broadband super-planckian thermal emission from hyperbolic metamaterials, *Applied Physics Letters* **101**, 131106 (2012).
 - [8] S.-A. Biehs, M. Tschikin, R. Messina, and P. Ben-Abdallah, Super-planckian near-field thermal emission with phonon-polaritonic hyperbolic metamaterials, *Applied Physics Letters* **102**, 131106 (2013).
 - [9] J. Yang, W. Du, Y. Su, Y. Fu, S. Gong, S. He, and Y. Ma, Observing of the super-planckian near-field thermal radiation between graphene sheets, *Nature communications* **9**, 1 (2018).
 - [10] M. S. Mirmoosa, S.-A. Biehs, and C. R. Simovski, Superplanckian thermophotovoltaics without vacuum gaps, *Physical Review Applied* **8**, 054020 (2017).
 - [11] X. Liu, R. Zhang, and Z. Zhang, Near-field radiative heat transfer with doped-silicon nanostructured metamaterials, *International Journal of Heat and Mass Transfer* **73**, 389 (2014).
 - [12] X. Liu, R. Zhang, and Z. Zhang, Near-field thermal radiation between hyperbolic metamaterials: Graphite and carbon nanotubes, *Applied Physics Letters* **103**, 213102 (2013).
 - [13] S.-A. Biehs, P. Ben-Abdallah, F. S. Rosa, K. Joulain, and J.-J. Greffet, Nanoscale heat flux between nanoporous materials, *Optics express* **19**, A1088 (2011).
 - [14] D. A. Somers, J. L. Garrett, K. J. Palm, and J. N. Munday, Measurement of the casimir torque, *Nature* **564**, 386 (2018).
 - [15] A. Ott, P. Ben-Abdallah, and S.-A. Biehs, Circular heat and momentum flux radiated by magneto-optical nanoparticles, *Physical Review B* **97**, 205414 (2018).
 - [16] C. Khandekar and Z. Jacob, Circularly polarized thermal radiation from nonequilibrium coupled antennas, *Physical Review Applied* **12**, 014053 (2019).
 - [17] K. Y. Bliokh, F. J. Rodríguez-Fortuño, F. Nori, and A. V. Zayats, Spin-orbit interactions of light, *Nature Photonics* **9**, 796 (2015).
 - [18] A. Ott and S.-A. Biehs, Thermal rectification and spin-spin coupling of nonreciprocal localized and surface modes, *Physical Review B* **101**, 155428 (2020).
 - [19] G. Armelles, A. Cebollada, A. García-Martín, and M. U. González, Magnetoplasmonics: combining magnetic and plasmonic functionalities, *Advanced Optical Materials* **1**,

- 10 (2013).
- [20] P. Sengupta, C. Khandekar, T. Van Mechelen, R. Rahman, and Z. Jacob, Electron g-factor engineering for non-reciprocal spin photonics, *Physical Review B* **101**, 035412 (2020).
 - [21] A. Ishimaru, *Electromagnetic wave propagation, radiation, and scattering: from fundamentals to applications* (John Wiley & Sons, 2017).
 - [22] O. V. Kotov and Y. E. Lozovik, Giant tunable nonreciprocity of light in weyl semimetals, *Physical Review B* **98**, 195446 (2018).
 - [23] L. Zhu and S. Fan, Near-complete violation of detailed balance in thermal radiation, *Physical Review B* **90**, 220301(R) (2014).
 - [24] I. Latella and P. Ben-Abdallah, Giant thermal magnetoresistance in plasmonic structures, *Physical review letters* **118**, 173902 (2017).
 - [25] P. Ben-Abdallah, Photon thermal hall effect, *Physical review letters* **116**, 084301 (2016).
 - [26] F. Herz and S.-A. Biehs, Green-kubo relation for thermal radiation in non-reciprocal systems, *EPL (Europhysics Letters)* **127**, 44001 (2019).
 - [27] E. Moncada-Villa, V. Fernández-Hurtado, F. J. Garcia-Vidal, A. García-Martín, and J. C. Cuevas, Magnetic field control of near-field radiative heat transfer and the realization of highly tunable hyperbolic thermal emitters, *Physical Review B* **92**, 125418 (2015).
 - [28] T. Van Mechelen and Z. Jacob, Quantum gyroelectric effect: Photon spin-1 quantization in continuum topological bosonic phases, *Physical Review A* **98**, 023842 (2018).
 - [29] C. Khandekar and Z. Jacob, Thermal spin photonics in the near-field of nonreciprocal media, *New Journal of Physics* **21**, 103030 (2019).
 - [30] C. Khandekar, Z. Li, and Z. Jacob, Universal spin-resolved kirchhoff's laws of thermal radiation for nonreciprocal planar media, *arXiv preprint arXiv:1912.07177* (2019).
 - [31] M. Krüger, T. Emig, and M. Kardar, Nonequilibrium electromagnetic fluctuations: Heat transfer and interactions, *Physical Review Letters* **106**, 210404 (2011).
 - [32] M. Krüger, G. Bimonte, T. Emig, and M. Kardar, Trace formulas for nonequilibrium casimir interactions, heat radiation, and heat transfer for arbitrary objects, *Physical Review B* **86**, 115423 (2012).
 - [33] A. W. Rodriguez, M. T. H. Reid, and S. G. Johnson, Fluctuating-surface-current formulation of radiative heat transfer for arbitrary geometries, *Physical Review B* **86**, 220302(R) (2012).
 - [34] A. W. Rodriguez, M. T. H. Reid, and S. G. Johnson, Fluctuating-surface-current formulation of radiative heat transfer: theory and applications, *Physical Review B* **88**, 054305 (2013).
 - [35] A. G. Polimeridis, M. T. H. Reid, W. Jin, S. G. Johnson, J. K. White, and A. W. Rodriguez, Fluctuating volume-current formulation of electromagnetic fluctuations in inhomogeneous media: Incandescence and luminescence in arbitrary geometries, *Physical Review B* **92**, 134202 (2015).
 - [36] S. Edalatpour and M. Francoeur, The thermal discrete dipole approximation (t-dda) for near-field radiative heat transfer simulations in three-dimensional arbitrary geometries, *Journal of Quantitative Spectroscopy and Radiative Transfer* **133**, 364 (2014).
 - [37] S. Edalatpour, M. Čuma, T. Trueax, R. Backman, and M. Francoeur, Convergence analysis of the thermal discrete dipole approximation, *Physical Review E* **91**, 063307 (2015).
 - [38] R. M. Abraham Ekeröth, A. García-Martín, and J. C. Cuevas, Thermal discrete dipole approximation for the description of thermal emission and radiative heat transfer of magneto-optical systems, *Physical Review B* **95**, 235428 (2017).
 - [39] D. Polder and M. Van Hove, Theory of radiative heat transfer between closely spaced bodies, *Physical Review B* **4**, 3303 (1971).
 - [40] C. T. Schmiegelow and F. Schmidt-Kaler, Light with orbital angular momentum interacting with trapped ions, *The European Physical Journal D* **66**, 157 (2012).
 - [41] C. T. Schmiegelow, J. Schulz, H. Kaufmann, T. Ruster, U. G. Poschinger, and F. Schmidt-Kaler, Transfer of optical orbital angular momentum to a bound electron, *Nature communications* **7**, 12998 (2016).
 - [42] S. Urazhdin, V. Demidov, H. Ulrichs, T. Kendziorczyk, T. Kuhn, J. Leuthold, G. Wilde, and S. Demokritov, Nanomagnonic devices based on the spin-transfer torque, *Nature nanotechnology* **9**, 509 (2014).
 - [43] D. C. Ralph and M. D. Stiles, Spin transfer torques, *Journal of Magnetism and Magnetic Materials* **320**, 1190 (2008).
 - [44] C. Guo, B. Zhao, D. Huang, and S. Fan, Radiative thermal router based on tunable magnetic weyl semimetals, *ACS Photonics* (2020).
 - [45] B. Zhao, C. Guo, C. A. Garcia, P. Narang, and S. Fan, Axion-field-enabled nonreciprocal thermal radiation in weyl semimetals, *Nano Letters* **20**, 1923 (2020).
 - [46] Y. Tsurimaki, X. Qian, S. Pajovic, F. Han, M. Li, and G. Chen, Large nonreciprocal absorption and emission of radiation in type-i weyl semimetals with time reversal symmetry breaking, *Physical Review B* **101**, 165426 (2020).
 - [47] S. M. Barnett, Optical angular-momentum flux, *Journal of Optics B: Quantum and Semiclassical Optics* **4**, S7 (2001).
 - [48] R. Messina, M. Tschikin, S.-A. Biehs, and P. Ben-Abdallah, Fluctuation-electrodynamics theory and dynamics of heat transfer in systems of multiple dipoles, *Physical Review B* **88**, 104307 (2013).
 - [49] A. Manjavacas and F. J. García de Abajo, Radiative heat transfer between neighboring particles, *Physical Review B* **86**, 075466 (2012).
 - [50] A. Hartstein, E. Burstein, E. Palik, R. Gammon, and B. Hennis, Investigation of optic-phonon—magnetoplasmon-type surface polaritons on n-insb, *Physical Review B* **12**, 3186 (1975).
 - [51] E. Palik, R. Kaplan, R. Gammon, H. Kaplan, R. Wallis, and J. Quinn, Coupled surface magnetoplasmon-optic-phonon polariton modes on insb, *Physical Review B* **13**, 2497 (1976).
 - [52] J. Chochol, K. Postava, M. Čada, M. Vanwolleghem, L. Halagačka, J.-F. Lampin, and J. Pištora, Magneto-optical properties of insb for terahertz applications, *AIP Advances* **6**, 115021 (2016).
 - [53] J. Chochol, K. Postava, M. Čada, and J. Pištora, Experimental demonstration of magnetoplasmon polariton at insb (inas)/dielectric interface for terahertz sensor application, *Scientific Reports* **7**, 1 (2017).
 - [54] S. M. Barnett, L. Allen, R. P. Cameron, C. R. Gilson,

- M. J. Padgett, F. C. Speirits, and A. M. Yao, On the natures of the spin and orbital parts of optical angular momentum, *Journal of Optics* **18**, 064004 (2016).
- [55] K. Y. Bliokh, J. Dressel, and F. Nori, Conservation of the spin and orbital angular momenta in electromagnetism, *New Journal of Physics* **16**, 093037 (2014).
- [56] R. P. Cameron, S. M. Barnett, and A. M. Yao, Optical helicity, optical spin and related quantities in electromagnetic theory, *New Journal of Physics* **14**, 053050 (2012).
- [57] A. Manjavacas and F. J. García de Abajo, Thermal and vacuum friction acting on rotating particles, *Physical Review A* **82**, 063827 (2010).
- [58] R. Zhao, A. Manjavacas, F. J. García de Abajo, and J. Pendry, Rotational quantum friction, *Physical review letters* **109**, 123604 (2012).
- [59] A. Manjavacas and F. J. García de Abajo, Vacuum friction in rotating particles, *Physical review letters* **105**, 113601 (2010).
- [60] Z. Xu, Z. Jacob, and T. Li, Enhancement of rotational vacuum friction by surface photon tunneling, *Nanophotonics*, 20200391 (18 Sep. 2020).
- [61] N. Shitrit, I. Yulevich, E. Maguid, D. Ozeri, D. Veksler, V. Kleiner, and E. Hasman, Spin-optical metamaterial route to spin-controlled photonics, *Science* **340**, 724 (2013).
- [62] C. Wu, N. Arju, G. Kelp, J. A. Fan, J. Dominguez, E. Gonzales, E. Tutuc, I. Brener, and G. Shvets, Spectrally selective chiral silicon metasurfaces based on infrared fano resonances, *Nature communications* **5**, 1 (2014).
- [63] J. Ahn, Z. Xu, J. Bang, P. Ju, X. Gao, and T. Li, Ultra-sensitive torque detection with an optically levitated nanorotor, *Nature Nanotechnology* **15**, 89 (2020).
- [64] Y. Guo and S. Fan, A single gyrotropic particle as a heat engine, *arXiv preprint arXiv:2007.11234* (2020).
- [65] T. M. Hoang, Y. Ma, J. Ahn, J. Bang, F. Robicheaux, Z.-Q. Yin, and T. Li, Torsional optomechanics of a levitated nonspherical nanoparticle, *Physical review letters* **117**, 123604 (2016).
- [66] J. Ahn, Z. Xu, J. Bang, Y.-H. Deng, T. M. Hoang, Q. Han, R.-M. Ma, and T. Li, Optically levitated nanodumbbell torsion balance and ghz nanomechanical rotor, *Physical review letters* **121**, 033603 (2018).
- [67] J. Mun, M. Kim, Y. Yang, T. Badloe, J. Ni, Y. Chen, C.-W. Qiu, and J. Rho, Electromagnetic chirality: from fundamentals to nontraditional chiroptical phenomena, *Light: Science & Applications* **9**, 139 (2020).
- [68] Z. Xu and T. Li, Detecting casimir torque with an optically levitated nanorod, *Physical Review A* **96**, 033843 (2017).
- [69] R. Guérout, C. Genet, A. Lambrecht, and S. Reynaud, Casimir torque between nanostructured plates, *EPL (Europhysics Letters)* **111**, 44001 (2015).
- [70] K. Sinha, Repulsive vacuum-induced forces on a magnetic particle, *Phys. Rev. A* **97**, 032513 (2018).
- [71] P. Kim, B. Hauer, C. Doolin, F. Souris, and J. Davis, Approaching the standard quantum limit of mechanical torque sensing, *Nature communications* **7**, 1 (2016).
- [72] A. Lakhtakia, General theory of the purcell-pennypacker scattering approach and its extension to bianisotropic scatterers, *The Astrophysical Journal* **394**, 494 (1992).
- [73] A. D. Yaghjian, Electric dyadic green's functions in the source region, *Proceedings of the IEEE* **68**, 248 (1980).